Evaluation of the electric quadrupole shift in the ytterbium single-ion optical clock

Chao-Wei Wang(王潮巍), Shao-Yang Dai(戴少阳), Ya-Ni Zuo(左娅妮), Kun Liu(刘昆), Wen-Bo Zhao(赵文博), Yue-Xiang Han(韩越祥), Fang Fang(房芳)

Citation: Chin. Phys. B. 35, 103201 (2026). DOI: 10.1088/1674-1056/ae60eb | CSTR: 32038.14.CPB.ae60eb
http://cpb.iphy.ac.cn; http://iopscience.iop.org/cpb

What follows is a list of articles you may be interested in

Electric field intensity measurement by using doublet electromagnetically induced transparency of cold Rb Rydberg atoms

Ting Gong(宫廷), Shuai Shi(师帅), Zhonghua Ji(姬中华), Guqing Guo(郭古青), Xiaocong Sun(孙小聪), Yali Tian(田亚莉), Xuanbing Qiu(邱选兵), Chuanliang Li(李传亮), Yanting Zhao(赵延霆), Suotang Jia(贾锁堂)

Chin. Phys. B. 32, 103202 (2023). DOI: 10.1088/1674-1056/acf120

Atom-based power-frequency electric field measurement using the radio-frequency-modulated Rydberg spectroscopy

Weixin Liu(刘伟新), Linjie Zhang(张临杰), Tao Wang(汪涛)

Chin. Phys. B. 32, 053203 (2023). DOI: 10.1088/1674-1056/aca6db

Rydberg electromagnetically induced transparency and Autler-Townes splitting in a weak radio-frequency electric field

Liping Hao(郝丽萍), Yongmei Xue(薛咏梅), Jiabei Fan(樊佳蓓), Yuechun Jiao(焦月春), Jianming Zhao(赵建明), Suotang Jia(贾锁堂)

Chin. Phys. B. 28, 053202 (2019). DOI: 10.1088/1674-1056/28/5/053202

Quantum photodetachment of hydrogen negative ion in a harmonic potential subjected to static electric field

Azmat Iqbal, Kiran Humayun, Sana Maqsood, Saba Jawaid, Afaq Ahmad, Amin Ur Rahman, Bakht Amin Bacha

Chin. Phys. B. 28, 023201 (2019). DOI: 10.1088/1674-1056/28/2/023201

Evaluation of the electric quadrupole shift in the ytterbium single-ion optical clock

Chao-Wei Wang(王潮巍)[1,2], Shao-Yang Dai(戴少阳)[2,3,4,†], Ya-Ni Zuo(左娅妮)[2,3,4], Kun Liu(刘昆)[2,4], Wen-Bo Zhao(赵文博)[2], Yue-Xiang Han(韩越祥)[2], and Fang Fang(房芳)[2,3,5,‡]

[1] *Department of Precision Machinery and Precision Instruments, School of Engineering Science, University of Science and Technology of China, Hefei* 230022, *China*
[2] *Time and Frequency Division, National Institute of Metrology, Beijing* 100029, *China*
[3] *Hefei National Laboratory, Hefei* 230088, *China*
[4] *Key Laboratory of Time Frequency and Gravity Primary Standard, State Administration for Market Regulation, Beijing* 100029, *China*
[5] *Beijing Key Laboratory of Quantum Metrology Technology and Instruments, Beijing* 100029, *China*

(Received 30 December 2025; revised manuscript received 4 April 2026; accepted manuscript online 17 April 2026)

Optical clocks with ultralow uncertainty are strong candidates for the next redefinition of the SI second. The $^{171}Yb^{+}$ single-ion clock is particularly attractive owing to its two clock transitions (E2 and E3) and its potential for low uncertainty. A major contribution to the uncertainty budget arises from the electric-quadrupole shift, caused by the interaction between the atomic quadrupole moment and the electric-field gradient at the trap center and strongly dependent on the orientation of the quantization axis. To evaluate this shift, a simplified orthogonal magnetic-field method was employed: three mutually orthogonal magnetic-field directions are generated together with an auxiliary non-orthogonal field. With a dual-condition locking scheme, we measure the E2 transition frequency differences between magnetic-field configurations, infer the electric-field gradient, and apply corrections for the associated quadratic Zeeman shifts. The uncertainty due to magnetic-field misalignment is quantified using a calibrated current-to-field model. The resulting electric-quadrupole shift correction for the $^{2}S_{1/2} \rightarrow {}^{2}F_{7/2}$ (E3) transition is 3.24 mHz, corresponding to a fractional uncertainty of 1.1×10^{-18} in the absolute frequency measurement.

Keywords: ytterbium ion optical clock, electric-quadrupole shift, uncertainty evaluation

PACS: 32.10.Dk, 32.60.+i, 06.30.Ft, 37.10.Ty

DOI: 10.1088/1674-1056/ae60eb **CSTR:** 32038.14.CPB.ae60eb

1. Introduction

With rapid progress in optical frequency standards, single-ion optical clocks have become leading candidates for a future redefinition of the SI second due to their excellent stability and accuracy.[1–6] The $^{171}Yb^{+}$ optical clock is of particular interest as it provides two independent clock transitions, namely the electric-quadrupole (E2) and electric-octupole (E3) transitions.[7–11] In particular, the E3 transition has achieved a systematic uncertainty at the 10^{-18} level.[12,13] Among the systematic effects relevant to high-accuracy operation, the electric-quadrupole shift is one of the most critical contributions.[13–16] It originates from the interaction between the atomic electric-quadrupole moment and the electric-field gradient at the trap center.[17] This effect depends strongly on the angle between the electric-field gradient axis and the quantization axis, making its evaluation and control essential for achieving high clock accuracy.

Several approaches have been developed to suppress or evaluate the electric-quadrupole shift. Itano first proposed cancelling the shift by averaging over different magnetic-field orientations,[17] which has been implemented in several different kinds of ion optical frequency standards such as $^{87}Sr^{+}$, $^{171}Yb^{+}$, and $^{199}Hg^{+}$,[18–21] reaching quadrupole shift uncertainties as low as 2.2×10^{-17}. Subsequently, Dube *et al.*[14] introduced a method based on combining Zeeman components under a fixed magnetic field, reducing the associated uncertainty to 5.0×10^{-18}. Shaniv *et al.*[22] later proposed dynamic-decoupling radio-frequency pulse sequences to suppress the quadrupole shift during interrogation. More recently, Lange *et al.*[23] implemented a rotating magnetic field within a Ramsey sequence and demonstrated suppression of the $^{171}Yb^{+}$ E3 quadrupole shift at the 10^{-20} level. In this work, we adopt the orthogonal-field method because it is directly compatible with the existing $^{171}Yb^{+}$ clock system and is well suited to a relatively simple static evaluation of the quadrupole shift under the operating magnetic field. Unlike rotating-field schemes, which are advantageous for in-cycle tensor-shift suppression during Ramsey interrogation, the present approach relies only on several static magnetic-field configurations generated by the available coil system and enables explicit characterization of the local field gradient related direction together with a quantitative uncertainty analysis. However, its performance

†Corresponding author. E-mail: daisy@nim.ac.cn
‡Corresponding author. E-mail: fangf@nim.ac.cn

© 2026 Chinese Physical Society and IOP Publishing Ltd. All rights, including for text and data mining, AI training, and similar technologies, are reserved.

depends on how accurately the magnetic-field directions are realized. We therefore calibrate both the field amplitudes and orientations by fitting a Jacobian current-to-field matrix and the background field using 64 current–field data sets. This calibration reduces the angular uncertainty to 0.2°, corresponding to an uncertainty contribution below 0.02 mHz in the final electric-quadrupole shift budget. In our system, the dominant contribution is measurement repeatability. We then present an experimental evaluation of the E3 electric-quadrupole shift in the $^{171}Yb^{+}$ optical clock developed at the National Institute of Metrology (NIM), China, including corrections for the second-order Zeeman shift and a quantitative uncertainty budget. This study provides an experimental basis for evaluating the electric quadrupole shift in Yb^{+} optical clocks and establishes a foundation for further reduction of systematic uncertainties.

2. Experimental setup

2.1. Ion trap and optical system

The experiment was conducted on the NIM-Yb1 single-ion optical clock platform developed at NIM. The ion trap employs an end-cap structure with an electrode spacing of approximately 1 mm.[24,25] The trap is driven at 15.179 MHz with a typical radio frequency (RF) voltage amplitude of around 600 V, providing stable confinement of a single $^{171}Yb^{+}$ ion under ultrahigh vacuum below 10^{-8} Pa. The ion is produced via photoionization using a 399 nm laser and a 369.5 nm laser. Doppler cooling is performed on the 369.5 nm transition,[26] with repumping lasers at 935 nm and 760 nm to depopulate metastable states. Interrogation of the $^{2}S_{1/2}$ ($F=0$) $\rightarrow$ $^{2}D_{3/2}$ ($F=2$) (E2) transition at 435 nm is performed using an ultrastable laser locked to a 100 mm ULE cavity.[27] With a 30 ms Rabi pulse, a spectral linewidth of approximately 26 Hz is obtained.

2.2. Configuration of three-dimensional magnetic fields

To generate and control three mutually orthogonal magnetic fields, three pairs of Helmholtz coils are installed along the laboratory X, Y, and Z axes (see Fig. 1). The geometric center of the coil pairs is aligned with the ion position to ensure good field uniformity at the trap center. In each Helmholtz pair, the two coils are connected in series. During clock interrogation, each series-connected coil pair is driven by two low-noise current sources (Keithley 6220), which are used as a constant base-current channel and a switchable differential-current channel, respectively, with a current noise below 20 μA. This arrangement allows fast and reproducible switching between preset magnetic-field configurations during interleaved measurements, while keeping the reference current unchanged. By combining the base currents and differential currents of the three coil pairs, an arbitrary magnetic-field vector can be synthesized for setting the quantization axis. For the y-axis coil pair, an additional high-field current source is used only during cooling, state preparation, and detection; it is switched off during clock interrogation and is not included in the current vector discussed later.

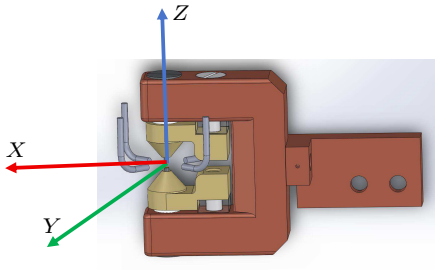

Fig. 1. The ion trap used in the laboratory and the corresponding coordinate system definition.

3. Theoretical analysis

3.1. Electric quadrupole shift

In the $^{171}Yb^{+}$ optical clock, the ground state $^{2}S_{1/2}$ ($F=0$) is spherically symmetric and therefore has no electric-quadrupole moment. By contrast, the excited states $^{2}D_{3/2}$ ($F=2$) and $^{2}F_{7/2}$ ($F=3$) possess nonzero quadrupole moments, which leads to an energy shift in the presence of an external electric-field gradient. For a hyperfine state $|\gamma IJFM_F\rangle$, the quadrupole shift can be written as[17]

$$\Delta\nu_q = \frac{G}{h}k(J,I,F,m_F)\Theta(\gamma,J)[(3\cos^2\beta-1) - \epsilon\sin^2\beta(\cos^2\alpha-\sin^2\alpha)]. \quad (1)$$

This expression follows from first-order perturbation theory under the usual condition that the Zeeman splitting induced by the applied magnetic field (typically at the 10 kHz level) is much larger than the quadrupole interaction (typically at the mHz level). Here, γ denotes the electronic configuration of the atom; I is the nuclear spin, J the total electronic angular momentum, F the total angular momentum, and m_F its projection on the quantization axis. The angles α and β describe the orientation of the field-gradient principal axis relative to the quantization axis defined by the magnetic field, where β represents the angle between the principal axis of the electric-field gradient and the quantization axis, and α denotes the rotation angle around the quantization axis. G parameterizes the field-gradient strength,[14] ϵ quantifies a small departure from the ion trap's cylindrical symmetry due to fabrication or alignment.[28] For an endcap Paul trap[25,29] as in Fig. 1, it is typically negligible.[30,31]

For the E2 ($^{2}D_{3/2}$ ($F=2$)) and E3 ($^{2}F_{7/2}$ ($F=3$)) clock states of $^{171}Yb^{+}$, the measured quadrupole moments are $\Theta(D,3/2)=1.95(1)ea_0^2$ and $\Theta(F,7/2)=-0.0297(5)ea_0^2$, respectively, with the corresponding angular factors $k=1$ and

$k = 5/7$.[23] Here, e is the elementary charge and a_0 is the Bohr radius.

Therefore, the electric quadrupole shift can be more simply expressed as

$$\Delta\nu_q = \frac{\Delta\nu_{q\max}}{2}\left(3\cos^2\beta - 1\right), \tag{2}$$

where $\Delta\nu_{q\max}$ is the maximum electric quadrupole shift when the magnetic field is aligned with the electric-field gradient.

3.2. Magnetic field vector model

To control the quantization axis accurately, we model the total magnetic field at the ion as the sum of a static background field and the fields generated by the three coil pairs. Because the mapping from coil currents to the field components is determined by the coil geometry and is essentially time-invariant, we describe it using a Jacobian matrix model:

$$\boldsymbol{B}(\boldsymbol{I}) = \boldsymbol{A}\boldsymbol{I} + \boldsymbol{B}_0 \equiv \begin{bmatrix} \frac{\partial B_{\hat{x}}}{\partial I_1} & \frac{\partial B_{\hat{x}}}{\partial I_2} & \frac{\partial B_{\hat{x}}}{\partial I_3} \\ \frac{\partial B_{\hat{y}}}{\partial I_1} & \frac{\partial B_{\hat{y}}}{\partial I_2} & \frac{\partial B_{\hat{y}}}{\partial I_3} \\ \frac{\partial B_{\hat{z}}}{\partial I_1} & \frac{\partial B_{\hat{z}}}{\partial I_2} & \frac{\partial B_{\hat{z}}}{\partial I_3} \end{bmatrix} \begin{bmatrix} I_1 \\ I_2 \\ I_3 \end{bmatrix} + \begin{bmatrix} B_{0,\hat{x}} \\ B_{0,\hat{y}} \\ B_{0,\hat{z}} \end{bmatrix}, \tag{3}$$

where $\boldsymbol{B}_0$ is the background magnetic-field vector, $\boldsymbol{I}$ is the current vector, and $\boldsymbol{A}$ is the Jacobian matrix relating coil currents to field components.

Since the $\hat{x}$–$\hat{y}$–$\hat{z}$ magnetic-field coordinate system is not known a priori, all 12 coefficients in this model are not uniquely defined unless a coordinate convention is imposed. Although the magnetic-field directions produced by the three coil pairs, $\hat{\boldsymbol{n}}_1$, $\hat{\boldsymbol{n}}_2$, and $\hat{\boldsymbol{n}}_3$, are designed to align with the laboratory coordinate system (x–y–z) shown in Fig. 1, small misalignments and cross-couplings are unavoidable. We therefore construct an orthogonal coordinate system for field characterization, as shown in Fig. 2:[32]

$$\hat{\boldsymbol{x}} = \hat{\boldsymbol{n}}_1, \quad \hat{\boldsymbol{y}} = \hat{\boldsymbol{z}} \times \hat{\boldsymbol{n}}_1, \quad \hat{\boldsymbol{z}} = \frac{\hat{\boldsymbol{n}}_1 \times \hat{\boldsymbol{n}}_2}{|\hat{\boldsymbol{n}}_1 \times \hat{\boldsymbol{n}}_2|}. \tag{4}$$

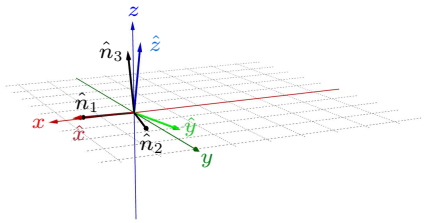

Fig. 2. The three-dimensional orthogonal coordinate system ($\hat{x}$–$\hat{y}$–$\hat{z}$) defined by the actual orientations of the coils, with the tilting of the coil orientations exaggerated for clarity.

In this coordinate system, $\partial B_{\hat{y}}/\partial I_1 = \partial B_{\hat{z}}/\partial I_1 = \partial B_{\hat{z}}/\partial I_2 = 0$, so $\boldsymbol{A}$ becomes upper-triangular (Eq. (5)), which simplifies parameter estimation and enables us to calculate the currents required to realize a set of orthogonal field vectors used in the quadrupole-shift cancellation strategy.

$$\boldsymbol{A} = \begin{bmatrix} \frac{\partial B_{\hat{x}}}{\partial I_1} & \frac{\partial B_{\hat{x}}}{\partial I_2} & \frac{\partial B_{\hat{x}}}{\partial I_3} \\ 0 & \frac{\partial B_{\hat{y}}}{\partial I_2} & \frac{\partial B_{\hat{y}}}{\partial I_3} \\ 0 & 0 & \frac{\partial B_{\hat{z}}}{\partial I_3} \end{bmatrix}. \tag{5}$$

4. Measurement method

4.1. Orthogonal-field strategy

When the clock transition is probed under three mutually orthogonal magnetic-field directions ($i = 1, 2, 3$), the electric-field gradient can be treated as a vector in the orthogonal magnetic coordinate system. For an ideal orthogonal triad, the geometric factors satisfy[33]

$$\sum_i^3 \cos^2\beta_i = 1, \tag{6}$$

and the quadrupole shift for each field direction can be related:

$$\Delta\nu_{qi} = f_i - \sum_i^3 f_i/3, \tag{7}$$

where f_i denotes the measured clock transition frequency under the i-th magnetic-field setting. For convenience, the magnetic-field orientations used in this work are illustrated in Fig. 3. The field used for E3 interrogation is $\boldsymbol{B}_{\hat{y}} = (0, 3, 0)$ μT, which serves as B_2 among the three orthogonal magnetic fields, while B_1 and B_3 have the same magnitude and are directed along $(\sqrt{3}/2, 0, 1/2)$ and $(-1/2, 0, \sqrt{3}/2)$, respectively. In addition, an auxiliary field B_4 that is non-orthogonal to B_1, B_2, and B_3 is introduced to enable determination of the electric-field-gradient direction (see Subsection 6.3).

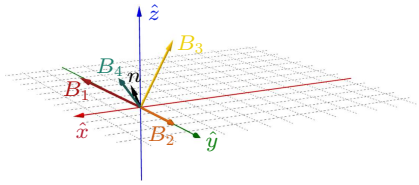

Fig. 3. Magnetic field orientations used for measuring the electric quadrupole shift, where B_1, B_2, and B_3 are mutually orthogonal, and B_4 is an auxiliary magnetic field non-orthogonal to all of them.

4.2. Dual-condition locking sequence

During E3 operation, the clock frequency often needs to be compared with other optical standards, in which case repeatedly changing the magnetic-field direction would complicate the evaluation of field-dependent frequency shifts. We therefore interrogate the E3 transition under a single magnetic-field direction ($B_{\hat{y}}$). Consequently, the quadrupole shift corresponding to that specific field direction must be directly calculated for later correction.

To reject the linear frequency drift of the probe laser, we employ an interleaved (dual-condition) locking scheme. Under each magnetic-field condition, the servo locks to the central clock resonance, and the error signal is generated from the

two frequency-discrimination points on the right and left sides of the central peak. For one magnetic-field condition, the probing sequence is right–left–left–right. At each frequency point, 25 interrogations are performed and the excitation probability is averaged. Therefore, each condition contains 100 interrogations in total. The system is then switched to the other preset magnetic-field condition B_i, and the same procedure is repeated. In this work, the B_2–B_1 and B_2–B_3 measurements were implemented as two separate interleaved locks. In both cases, the two-condition subsequences were alternated in a 1221 order to suppress, to first order, the influence of common laser drift on the measured frequency difference between the two magnetic-field conditions.

For each series-connected Helmholtz pair, the base-current channel is preset to the value required for the $B_{\hat{y}}$ configuration, while a second channel provides the differential current needed to realize the other magnetic-field conditions. The differential-current path is enabled or disabled by a TTL-controlled switch, which allows rapid alternation between field configurations during the dual-condition locking sequence. For the y-axis pair, the additional high-field channel used during cooling, state preparation, and detection is turned off during clock interrogation.

The recorded frequency difference $\Delta_i = f_i - f_2$ is thus largely immune to common-mode laser drift. Then the electric quadrupole frequency shift under the $B_{\hat{y}}$ condition can be simply calculated:

$$\Delta\nu_{q\hat{y}} = \Delta\nu_{q2} = -\sum_i^3 \Delta_i/3. \tag{8}$$

Considering the difference in k-factors and quadrupole moments between the E2 and E3 transitions, the quadrupole shift of the E2 transition is $R = (\Theta(F,7/2)\cdot k_{\mathrm{E2}})/(\Theta(D,3/2)\cdot k_{\mathrm{E3}}) = -92(2)$ times larger than that of the E3 transition.[23] Thus, the highly sensitive E2 transition is used to infer the E3 quadrupole shift correction through $\Delta\nu_{q,\mathrm{E3}} = \Delta\nu_{q,\mathrm{E2}}/R$, where the uncertainty of R, determined by the uncertainties of the E2 and E3 quadrupole moments, is included in the final uncertainty of the E3 result.

5. Data analysis and results

5.1. Magnetic field calibration results

The magnitude of the magnetic field at the ion is determined from the Zeeman splitting between the two $^2\mathrm{S}_{1/2}$ $(F=0, m_F=0) \rightarrow {}^2\mathrm{D}_{3/2}$ $(F=2, m_F=+2)$ and $^2\mathrm{S}_{1/2}$ $(F=0, m_F=0) \rightarrow {}^2\mathrm{D}_{3/2}$ $(F=2, m_F=-2)$ sublevels of the E2 clock transition:[32]

$$\Delta\nu_{\mathrm{Zeeman}}/B = \Delta m_F \times 8.393\ \mathrm{kHz}/\mu\mathrm{T}. \tag{9}$$

We apply 64 different current configurations and measure the field magnitude for each case. The magnitudes range from 1 μT to 10 μT, matching the μT-level magnetic fields required for actual clock operation. The typical uncertainty of a single field point is on the order of 4×10^{-4} μT, and these uncertainties are used to calculate the weights w_i later. The Jacobian matrix $\boldsymbol{A}$ and the background field $\boldsymbol{B}_0$ are determined by a least-squares fit that minimizes the sum of weighted squared residuals $\sum_i R_i^2 w_i$, where $R_i = |\boldsymbol{A}\boldsymbol{I}_i + \boldsymbol{B}_0| - |\boldsymbol{B}_i|$. The measurement results are shown in Fig. 4:

$$\boldsymbol{B}_0 = (-1.554(2), 1.433(2), 0.427(2))\ \mu\mathrm{T}, \tag{10}$$

$$\boldsymbol{A} = \begin{bmatrix} 245.25(7) & 3.57(24) & 2.37(12) \\ 0(0) & 509.77(20) & -0.52(12) \\ 0(0) & 0(0) & 238.47(9) \end{bmatrix}, \tag{11}$$

$$\boldsymbol{A}^{-1} = \begin{bmatrix} 4.074(1) & -0.029(2) & -0.041(2) \\ 0(0) & 1.962(1) & 0.004(1) \\ 0(0) & 0(0) & 4.193(2) \end{bmatrix}. \tag{12}$$

Here, the quoted parameter uncertainties are derived from the covariance matrix of the fit, corresponding to one-standard-deviation uncertainties.

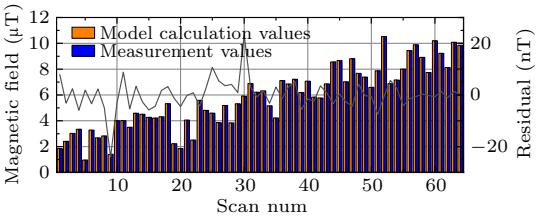

Fig. 4. Agreement between the calculated magnetic field values and the measured results from Zeeman spectrum locks across 64 different current configurations. The tested magnetic-field magnitudes range from 1 μT to 10 μT. The root mean square error of the model is 0.001998.

The current $\boldsymbol{I}$ required for a target magnetic field $\boldsymbol{B}$ is then

$$\boldsymbol{I} = \boldsymbol{A}^{-1}(\boldsymbol{B} - \boldsymbol{B}_0). \tag{13}$$

The near-diagonal structure of $\boldsymbol{A}$ indicates good orthogonality of the three coil pairs, with small cross-coupling at the $\sim 1\%$ level. Therefore, the fitted actual field directions $\hat{\boldsymbol{n}}_1$, $\hat{\boldsymbol{n}}_2$, and $\hat{\boldsymbol{n}}_3$ are close to the designed orthogonal magnetic coordinate system $\hat{x}$–$\hat{y}$–$\hat{z}$. For the $B_{\hat{y}}$ field required for the E3 transition, Eq. (13) yields $\boldsymbol{I} = (6.216, 3.060, -1.788)$ mA.

To characterize the coil settling time and magnetic-field fluctuations, we varied the preset delay between the magnetic-field switching and the probing pulse, and inferred the field magnitude from the locked E2 Zeeman splitting. As shown in Fig. 5, the magnetic field stabilizes approximately 25 ms after the coil current sources are enabled. In the experimental timing sequence, there is a 30 ms interval between the end of state preparation and the clock probing pulse. This interval is reserved for turning off the large magnetic field (~ 3 G) used during cooling, state preparation, and detection before interrogation begins.

In the experiment, the TTL signal controlling the magnetic-field switch is triggered simultaneously with the

turn-off of the large magnetic field. Therefore, the 30 ms interval ensures a stable field during interrogation. The linear model in Eq. (3) does not explicitly include magnetic hysteresis. However, no resolvable path-dependent offset is observed in the switching and long-term stability tests under the present operating conditions. Long-term locking measurements over 7 days (Fig. 6) show a peak-to-peak field variation of about 8.5 nT without any abnormal long-term drift. During this magnetic-field locking period, and during the subsequent clock-transition locking over about 7 days, the variations of all compensation-electrode voltages remained within 0.02 V, indicating that the local electric-field environment was stable throughout the experiment. The measured-field fluctuation is used to evaluate the DC second-order Zeeman shift contribution to the uncertainty budget, while the evaluation of oscillating magnetic fields is beyond the scope of the present work and does not constitute a dominant term at the current uncertainty level,[13] so it is not discussed separately.

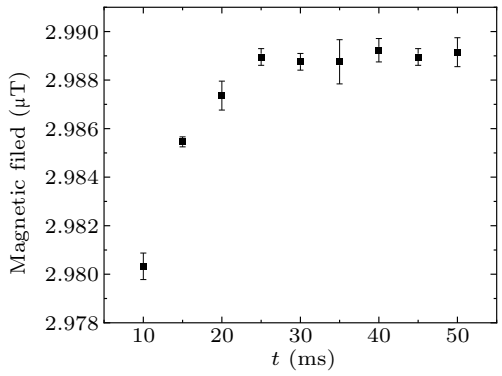

Fig. 5. Magnetic field inferred from locked E2 Zeeman splitting as a function of the preset delay between magnetic-field switching and the probing pulse. Each point is obtained from an independent locking measurement.

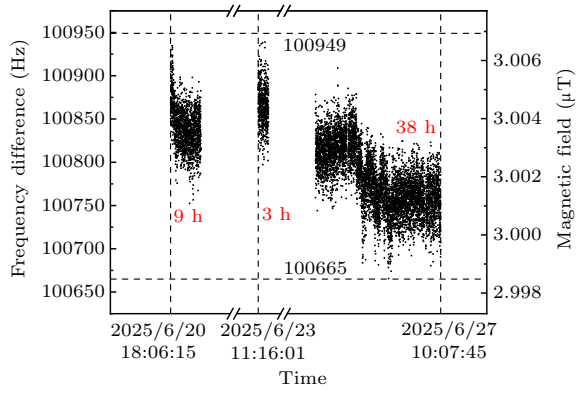

Fig. 6. Magnetic field stability test over a time span of 7 days, showing a peak-to-peak variation of 8.5 nT.

5.2. Second-order Zeeman shift correction

Since the magnetic-field magnitude cannot be guaranteed to be identical under different field conditions, the corresponding second-order Zeeman shift must be corrected. For the E2 transition, the shift can be expressed as

$$\Delta\nu_z = k_{\mathrm{E2}} B^2, \tag{14}$$

where $k_{\mathrm{E2}} = 52.13\,(9)$ mHz/μT^2.[34]

The measurement result Δ_i from the dual-condition locking described in Subsection 4.2 should then be corrected as follows:

$$f_i - f_2 = (\Delta\nu_{zi} - \Delta\nu_{z2}) + (\Delta\nu_{qi} - \Delta\nu_{q2}) = \Delta_i. \tag{15}$$

The corresponding electric quadrupole shift can be calculated using

$$\Delta\nu_{q2} = \frac{1}{3}\left[-\sum_{i=1}^{3}\Delta_i + \left(\sum_{i=1}^{3}\Delta\nu_{zi} - 3\Delta\nu_{z2}\right) + \sum_{i=1}^{3}\Delta\nu_{qi}\right], \tag{16}$$

$$\Delta\nu_{qi} = \Delta\nu_{q2} + \Delta_i - (\Delta\nu_{zi} - \Delta\nu_{z2}), \tag{17}$$

where the first term of Eq. (16) represents the sum of the measured values, the second term is the Zeeman shift correction, and the third term is theoretically zero. In matrix form, Eq. (17) can be further written as

$$\boldsymbol{\Delta\nu}_q = H_d \boldsymbol{d} + H_z \boldsymbol{z}, \tag{18}$$

where H_d and H_z are the coefficient matrices corresponding to the measured frequency shifts and the second-order Zeeman shifts, respectively, $\boldsymbol{d}$ is the vector of measured frequency shifts, and $\boldsymbol{z}$ is the vector of second-order Zeeman shifts.

5.3. Measurement results

Following the procedure above, dual-condition locking was performed for $f_1 - f_2$ and $f_3 - f_2$ for 255960 s and 59222 s, respectively. The corresponding calculated results are summarized in Table 1.

Table 1. Results of the dual-condition locking measurements under the three orthogonal magnetic-field conditions.

	B_1	B_2	B_3
Mean frequency difference $f_i - f_2$ (mHz)	518.36	0	371.38
Uncertainty of $f_i - f_2$ (mHz)	91.55	0	167.27
Magnetic-field magnitude (μT)	2.988	3.003	3.014
Uncertainty of magnetic-field magnitude (μT)	0.007	0.011	0.007
Second-order Zeeman shift $\Delta\nu_{\mathrm{s}}$ (mHz)	465.50	470.04	473.71
Uncertainty of $\Delta\nu_{\mathrm{s}}$ (mHz)	2.76	2.77	2.78

Using Eq. (16), the E2 electric quadrupole shift under $B_{\hat{y}}$ is calculated to be −296.87 mHz. The quadrupole shifts for other magnetic-field conditions are subsequently derived via Eq. (15). By scaling with R, the ratio of quadrupole moments and angular factors between E2 and E3, we obtain an E3 electric quadrupole shift of 3.24 mHz for the $B_{\hat{y}}$ operating field.

6. Uncertainty evaluation

The total uncertainty of the electric-quadrupole shift consists of three contributions (three parts of Eq. (16)): (i) statistical uncertainty of the measured frequency differences, (ii) uncertainty of the second-order Zeeman shift correction arising from field-magnitude errors and the coefficient uncertainty, and (iii) uncertainty due to imperfect orthogonality and finite

angular errors of the magnetic-field direction. The uncertainty evaluation follows the GUM framework.[35] We analyze each contribution below.

The following evaluation refers to a fixed operating configuration used in the present experiment. Here, except for switching the magnetic-field direction among the preset configurations, the trapped ion, micromotion-compensation setting, rf trapping condition, and the probe-beam geometry and polarization were kept unchanged during the comparison measurements. Under this condition, the probe-light Stark shift associated with the low-power (~ 5 nW) 435 nm E2 interrogation is negligible at the present evaluation level, while the rf-induced Stark shift mainly contributes an approximately common offset rather than an independent direction-dependent term. In addition, during the subsequent clock-transition locking over about 7 days, the variations of all compensation-electrode voltages remained within 0.02 V, and the ion was not reloaded. Under these conditions, changes in the electric-field gradient are not expected to contribute significantly at the present evaluation level. However, if the ion is reloaded after a long interruption and the compensation voltages are re-optimized over a large range (on the order of Volts), the resulting change in the electric-field gradient should be reconsidered and the evaluation repeated.

6.1. Measurement uncertainty

Allan deviations of the frequency differences are shown in Fig. 7. The statistical uncertainty is obtained directly from the dual-condition locking results. By extrapolating the data in Fig. 7, the relative uncertainties for $f_1 - f_2$ and $f_3 - f_2$ at their respective averaging times are determined to be 1.33×10^{-16} and 2.43×10^{-16}, respectively. This gives an uncertainty contribution of 63.56 mHz to the inferred E2 quadrupole shift for the $B_{\hat{y}}$ direction. The contribution is calculated from $H_d \Sigma_d H_d^{\mathrm{T}}$, where Σ_d denotes the covariance matrix of the measured frequency-difference vector, with the variances of the individual measurements placed on the diagonal.

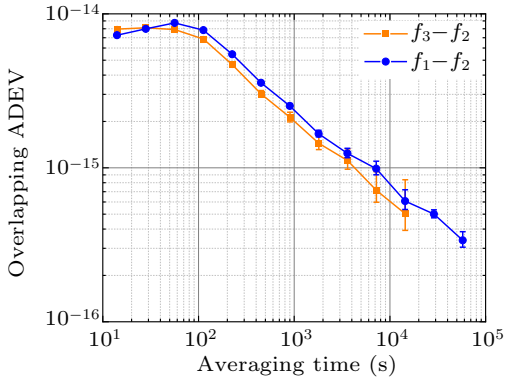

Fig. 7. Allan deviation for the two dual-condition locking measurements.

6.2. Uncertainty in second-order Zeeman shift correction

The uncertainty of the second-order Zeeman shift correction is evaluated from the measured field fluctuations in Fig. 6, the uncertainty of the magnetic field B propagated from Eq. (3), and the uncertainty of the Zeeman coefficient k_{E2}. For the three orthogonal magnetic fields, we obtain $u(\Delta\nu_{z1}) = 2.755$ mHz, $u(\Delta\nu_{z2}) = 2.770$ mHz, and $u(\Delta\nu_{z3}) = 2.781$ mHz, respectively. This gives an uncertainty contribution of 2.26 mHz from the second term in Eq. (16). The contribution is evaluated from $H_z \Sigma_z H_z^{\mathrm{T}}$, where Σ_z denotes the covariance matrix of the second-order Zeeman-shift vector.

6.3. Uncertainty in magnetic field orientation

Due to the current-source noise and the uncertainties of the fitted Jacobian matrix and background field, each synthesized magnetic-field direction has an angular uncertainty below 0.2°, according to Eq. (3).

The third term in Eq. (16), which is zero for an ideal orthogonal triad, is therefore treated as an uncertainty contribution arising from finite angular errors. It can be written as

$$\frac{1}{3}\sum_i^3 \Delta\nu_{qi} = \frac{\Delta\nu_{q\max}}{2}[(\cos^2\beta_1 + \cos^2\beta_2 + \cos^2\beta_3) - 1]. \quad (19)$$

To determine the uncertainty introduced by β_i, the magnitude of $\Delta\nu_{q\max}$ and the direction of the electric field gradient are required. Equation (2) can be rewritten as

$$\Delta\nu_q = \frac{|\boldsymbol{n}|}{2}\left(3\frac{(\boldsymbol{B}\cdot\boldsymbol{n})^2}{|\boldsymbol{B}|^2|\boldsymbol{n}|^2} - 1\right), \quad (20)$$

$$\boldsymbol{n} = \frac{2}{h}k(J,I,F,m_F)\Theta(\gamma,J)\boldsymbol{G}, \quad (21)$$

where $\boldsymbol{G}$ denotes the physical electric-field-gradient vector, and $\boldsymbol{n}$ is the corresponding scaled vector entering the quadrupole-shift expression, with unit Hz, and $|\boldsymbol{n}| = \Delta\nu_{q\max}$.

Thus, determining $\boldsymbol{n}$ allows evaluation of the impact of the uncertainty in the angle between the magnetic field and the electric-field gradient. Given the theoretically set magnetic-field directions and their corresponding measured quadrupole shifts, $\boldsymbol{n}$ can be fitted by minimizing the weighted residual sum

$$f_{\mathrm{fit}} = \sum\left[\frac{|\boldsymbol{n}|}{2}\left(\frac{3(\boldsymbol{n}\cdot\boldsymbol{B}_i)^2}{|\boldsymbol{n}|^2|\boldsymbol{B}_i|^2} - 1\right) - \Delta\nu_i\right]^2 \frac{1}{\sigma_i^2}. \quad (22)$$

Since three unknown parameters are involved, an auxiliary measurement under B_4 along (1, 1, 1) is added to fully constrain the fit. The configured current components and the calculated electric quadrupole shifts are listed in Table 2, where the large uncertainties in the shifts under B_3 and B_4 are mainly limited by the measurement time.

Table 2. Electric quadrupole shift under different magnetic-field conditions.

Parameters	B_1	B_2	B_3
$\hat{n}_1$ coil current (mA)	16.829(3)	6.216(2)	0.088(3)
$\hat{n}_2$ coil current (mA)	–2.819(3)	3.060(2)	–2.814(3)
$\hat{n}_3$ coil current (mA)	4.501(3)	–1.789(2)	9.107(3)
Electric quadrupole shift $\Delta\nu_{q,i}$ (mHz)	226.03	–296.87	70.84
Uncertainty of $\Delta\nu_{q,i}$ (mHz)	82.69	63.61	115.63

After applying the same procedure to B_4, the scaled vector obtained from fitting Eq. (22) is

$$\boldsymbol{n} = (0.2238\,(7), -0.1431\,(17), 0.6300\,(22))\ \text{Hz}.$$

The corresponding physical electric-field-gradient vector is then obtained from Eq. (20), and its relatively larger uncertainty mainly originates from the quadrupole moment coefficient $\Theta(\gamma, J)$:

$$\boldsymbol{G} = (84759\,(510), -54198\,(702), 238557\,(1484))\ \text{V/m}^2.$$

For comparison, the electric field gradient variation associated with the observed compensation voltage change ($\sim$0.02 V) is at the 500 V/m^2 level,[36] which is negligible relative to the fitted gradient magnitude.

Therefore, the angles between the fitted $\boldsymbol{n}$ and the three mutually orthogonal magnetic-field directions are $\beta_1 = 41.91\,(12)^\circ$, $\beta_2 = 102.09\,(13)^\circ$, and $\beta_3 = 50.63\,(7)^\circ$. The uncertainties of these angles are obtained by standard covariance propagation from the fitted vector $\boldsymbol{n}$ and the magnetic-field direction vectors,

$$\Sigma_{\boldsymbol{\beta}} = J_{\boldsymbol{\beta}} \Sigma_{nB} J_{\boldsymbol{\beta}}^{\mathrm{T}}, \tag{23}$$

where Σ_{nB} is the joint covariance matrix of the 12 components of $\boldsymbol{n}$ and the three orthogonal magnetic-field vectors, which contains the covariance matrix of the magnetic field, Σ_B, as a submatrix. And $J_{\boldsymbol{\beta}}$ is the Jacobian matrix of $(\beta_1, \beta_2, \beta_3)$ with respect to these 12 variables.

Subsequently, the uncertainty contribution arising from the third term in Eq. (16) is evaluated using the covariance-propagation formula in Eq. (24), yielding 1.31 mHz. Specifically,

$$u_{\mathrm{ang}}^2 = J_g \Sigma_{|\boldsymbol{n}|\boldsymbol{\beta}} J_g^{\mathrm{T}}, \tag{24}$$

where $\Sigma_{|\boldsymbol{n}|\boldsymbol{\beta}}$ is the joint covariance matrix of $|\boldsymbol{n}|$ and the three angles $(\beta_1, \beta_2, \beta_3)$, and J_g is the Jacobian matrix of Eq. (19) with respect to these four variables.

6.4. Total uncertainty budget

To account for the additional uncertainty caused by the slow drift of the background magnetic field during the clock-transition locking process, the background magnetic field was evaluated twice with an interval of 11 days. The difference between the corresponding electric-quadrupole shifts from the two evaluations, 8.61 mHz, is taken as the uncertainty associated with the slow drift of the background magnetic field B_0. This contribution is combined in quadrature in the final uncertainty budget.

The complete uncertainty budget is summarized in Table 3. The evaluation indicates that the corrected electric quadrupole shift for the E3 transition is 3.24 mHz (corresponding to a fractional shift of 5.0×10^{-18}), with a relative uncertainty of 1.1×10^{-18}, where measurement repeatability constitutes the dominant contribution. The effects of the second-order Zeeman shift correction and magnetic-field angular error are both at the 10^{-5} Hz level, contributing negligibly to the total uncertainty, which benefits from the long-term stability of the magnetic environment and the high orthogonality of the coil geometry. The overall evaluation is comparable to those reported by NPL and PTB,[37] indicating a high level of performance. Future reduction of the total uncertainty could be achieved by improving the signal-to-noise ratio of the clock laser lock and implementing more advanced methods for electric quadrupole shift cancellation.[22]

Table 3. Uncertainty budget of the electric-quadrupole shift.

Uncertainty source	E2 shift (10^{-18})	E2 uncertainty (10^{-18})	E3 shift (10^{-19})	E3 uncertainty (10^{-19})
Measurement	–430.9	92.3	50.3	10.8
$\Delta\nu_{\mathrm{Zeeman}}$ correction	–0.4	3.3	0.1	0.4
Angular uncertainty	0	1.9	0	0.2
B_0 drift	0	12.5	0	1.5
Total	–431.3	93.3	50.4	10.9

7. Conclusion and perspectives

This work presents an experimental evaluation and uncertainty analysis of the electric quadrupole shift for the E3 transition in the $^{171}\mathrm{Yb}^+$ single-ion optical clock system developed at NIM. Using a simplified three-orthogonal-field strategy together with an interleaved locking scheme on the E2 transition, we determine the quadrupole-shift correction for the E3 operating field. After accounting for second-order Zeeman shift corrections and magnetic-field orientation calibration, we obtain an E3 electric quadrupole shift correction of 3.24 mHz with a fractional uncertainty of 1.1×10^{-18}. The result is consistent with evaluations reported by leading laboratories (PTB

and NPL), confirming the reliability of the method and the stability of the system.

Future research will focus on further improving system stability and mitigating the electric quadrupole shift. On the one hand, enhancing the clock laser stability and the signal-to-noise ratio of the probe measurements can effectively reduce the uncertainty contribution from measurement repeatability. On the other hand, although the present orthogonal-field approach is simpler and more directly compatible with the current experimental system, its significant limitation is that the evaluation must be repeated when the experimental conditions change, for example after ion reloading, compensation-voltage re-optimization, or slow drifts of the local field environment. In contrast, techniques such as dynamic decoupling or Ramsey spectroscopy with a rotating magnetic field show promise for further suppressing residual tensor shifts in real time, laying the groundwork for further reduction of the systematic uncertainty in $^{171}Yb^{+}$ single-ion optical clocks.

Acknowledgements

This work is supported by the Quantum Science and Technology–National Science and Technology Major Project (Grant No. 2021ZD0300901), and the National Key Research and Development Program of China (Grant No. 2021YFF0603801), and the Basic Research Expenses Program of National Institute of Metrology of China (Grant Nos. AKYZD2411 and AKYKF2501).

References

[1] Dehmelt H G 1982 *IEEE Trans. Instrum. Meas.* **31** 83
[2] Gill P 2011 *Philos. Trans. R. Soc. A* **369** 4109
[3] Poli N, Oates C W, Gill P, *et al*. 2013 *Riv. Nuovo Cim.* **36** 555
[4] Riehle F 2015 *C. R. Phys.* **16** 506
[5] Ludlow A D, Boyd M M, Ye J, *et al*. 2015 *Rev. Mod. Phys.* **87** 637
[6] Marshall M C, Castillo D A R, Arthur-Dworschack W J, *et al.* 2025 *Phys. Rev. Lett.* **135** 033201
[7] Engelke D and Tamm C 1996 *Europhys. Lett.* **33** 347
[8] Roberts M, Taylor P, Barwood G P, *et al*. 1997 *Phys. Rev. Lett.* **78** 1876
[9] Tamm C, Engelke D and Buhner V 2000 *Phys. Rev. A* **61** 053405
[10] Stenger J, Tamm C, Haverkamp N, *et al*. 2001 *Opt. Lett.* **26** 1589
[11] Blythe P J, Webster S A, Margolis H S, *et al*. 2003 *Phys. Rev. A* **67** 020501
[12] Huntemann N, Sanner C, Lipphardt B, *et al*. 2016 *Phys. Rev. Lett.* **116** 063001
[13] Tofful A, Baynham C F A, Curtis E A, *et al*. 2024 *Metrologia* **61** 045001
[14] Dube P, Madej A A, Bernard J E, *et al*. 2005 *Phys. Rev. Lett.* **95** 033001
[15] Chwalla M, Benhelm J, Kim K, *et al*. 2009 *Phys. Rev. Lett.* **102** 023002
[16] Huang Y, Guan H, Liu P, *et al*. 2016 *Phys. Rev. Lett.* **116** 013001
[17] Itano W M 2000 *J. Res. Natl. Inst. Stand. Technol.* **105** 829
[18] Margolis H S, Barwood G P, Huang G, *et al*. 2004 *Science* **306** 1355
[19] Oskay W H, Itano W M and Bergquist J C 2005 *Phys. Rev. Lett.* **94** 163001
[20] Schneider T, Peik E and Tamm C 2005 *Phys. Rev. Lett.* **94** 230801
[21] Oskay W H, Diddams S A, Donley E A, *et al*. 2006 *Phys. Rev. Lett.* **97** 020801
[22] Shaniv R, Akerman N, Manovitz T, *et al*. 2019 *Phys. Rev. Lett.* **122** 223204
[23] Lange R, Huntemann N, Sanner C, *et al*. 2020 *Phys. Rev. Lett.* **125** 143201
[24] Nisbet-Jones P B R, King S A, Jones J M, *et al*. 2016 *Appl. Phys. B* **122** 57
[25] Wang C W, Dai S Y, Zuo Y N, *et al*. 2025 *AIP Adv.* **15** 055320
[26] Dai S Y, Wang C W, Cao S Y, *et al*. 2025 *AIP Adv.* **15** 075132
[27] Zhang Y N, Zuo Y N, Dai S Y, *et al*. 2025 *Acta Metrol. Sin.* **46** 899
[28] Brown L S and Gabrielse G 1982 *Phys. Rev. A* **25** 2423
[29] Schrama C A, Peik E, Smith W W, *et al*. 1993 *Opt. Commun.* **101** 32
[30] Madej A A, Bernard J E, Dube P, *et al*. 2004 *Phys. Rev. A* **70** 012507
[31] Barwood G P, Margolis H S, Huang G, *et al*. 2004 *Phys. Rev. Lett.* **93** 133001
[32] Baynham C F A 2018 *Frequency metrology at the 10^{-18} level with an ytterbium ion optical clock* (Ph.D. Dissertation) (University of Oxford)
[33] Arfken G B and Weber H J 2013 *Mathematical methods for physicists*, 7th edn. (Boston: Elsevier) p. 125
[34] Godun R M, Nisbet-Jones P B R, Jones J M, *et al*. 2014 *Phys. Rev. Lett.* **113** 210801
[35] Tao M, Ren S Y and Lao C J 2024 *Metrol. Sci. Technol.* **68** 40
[36] Schneider T 2005 *Optical frequency standard with a single $^{171}Yb^{+}$ ion* (Ph.D. Dissertation) (Hannover: Gottfried Wilhelm Leibniz Universitat Hannover)
[37] Lange R 2021 *High-Precision Frequency Comparisons and Searches for New Physics with Yb^{+} Optical Clocks* (Ph.D. Dissertation) (Hannover: Gottfried Wilhelm Leibniz Universitat Hannover)